Reviews of Electromagnetics, Vol. V, 2026
EuCAP 2026 Special Issue
DOI: 10.53792/RoE/2026/26006

Reviews of Electromagnetics
EuCAP 2026 Special Issue

Multi-Beam GRIN Luneburg Lens Antenna for Millimeter-Wave Radar Sensing

Mohammad Omid Bagheri[1]*, Veronica Leong[1], Justin Chow[1], Josh Visser[1], Yahia M. M. Antar[2], George Shaker[1]

Abstract
Compact millimeter-wave radar modules are attractive front ends for short-range sensing owing to their small form factor, low cost, and wide modulation bandwidth. Their embedded antennas, however, provide limited effective aperture, moderate gain, and broad fixed radiation characteristics, which constrain wide-angle sector-resolved sensing when several radar channels operate simultaneously. This paper presents a passive multi-beam tailored GRIN Luneburg lens antenna in which five commercial FMCW radar modules simultaneously excite a single shared aperture. Although a conventional Luneburg lens effectively focuses individual feeds, its purely radial phase profile is not optimized to control the composite electromagnetic response of multiple simultaneously excited off-axis commercial radar feeds. The proposed TLL introduces fabrication-aware non-radial volumetric phase control to reorganize this composite response into predefined sensing sectors while also improving adjacent-channel isolation near the design frequency. A 10-cm-diameter lens is designed and fabricated for five 58–63 GHz radar modules targeting sectors centered at -56°, -28°, 0°, $+28^\circ$, and $+56^\circ$, corresponding to approximately 140° of sectorized angular coverage. Under simultaneous five-port excitation, full-wave simulations show that the CLL composite response exhibits substantial central crowding and displaced sector maxima, whereas the TLL forms five dominant lobes near the prescribed directions with peak realized gains of approximately 20–22 dB. The TLL also produces frequency-selective adjacent-channel coupling minima of approximately -50 to -70 dB near 60 GHz. Experimental validation demonstrates approximately 10–13 dB received-power enhancement across the operating band together with threshold-based sector-selective target detection. These results demonstrate a passive shared-aperture approach for simultaneous multi-beam millimeter-wave radar sensing using commercial radar-module feeds.

Key terms
GRIN; Luneburg lens; Millimeter-wave; Multi-beam antenna; Passive beamforming; Radar sensing

[1] *Department of Electrical and Computer Engineering, University of Waterloo, Waterloo, Ontario, Canada*
[2] *Department of Electrical and Computer Engineering, Royal Military College of Canada, Kingston, Ontario, Canada*
*__Corresponding author__: omid.bagheri@uwaterloo.ca

Received: 19/06/2026, Accepted: 15/10/2026, Published: 09/11/2026

1. Introduction

Millimeter-wave radar sensing has shifted from bulky, application-specific platforms toward compact module-based front ends for short-range localization, target tracking, gesture recognition, and biomedical monitoring [1, 2, 3]. Commercial 60–80 GHz radar modules combine wide modulation bandwidth and fine range resolution with integrated transceiver circuitry, antennas, waveform generation, and baseband processing in miniature, low-cost packages [4, 5]. However, their embedded antennas provide limited effective aperture, moderate gain, and broad fixed radiation characteristics, restricting link budget, angular discrimination, and beam-shaping flexibility, particularly for wide-angle sector-resolved sensing.

Extending angular coverage conventionally requires mechanical beam scanning, electronically steered phased arrays, digital beamforming, frequency-scanned antennas, or reconfigurable apertures [6, 7, 8, 9]. Although effective, these approaches typically require moving parts, phase-control networks, additional RF or baseband hardware, synchronization, or calibration. Fixed multi-beam operation provides a passive alternative by illuminating predefined sectors simultaneously. Among passive aperture approaches, the GRIN Luneburg lens

is particularly suitable because its spherical refractive-index distribution maps different feed positions to different radiation directions, naturally supporting multi-feed, multi-beam operation. Related dielectric lenses [10, 11, 12, 13], engineered superstrates [14, 15, 16], metasurfaces [3, 17, 18, 19], and gradient-index structures [20] have likewise been used to enhance gain, shape radiation, focus electromagnetic energy, and enlarge the effective aperture of compact antennas and radar modules.

Multi-feed spherical Luneburg lenses are well established for generating simultaneous beams under controlled feed conditions. The 3D-printed millimeter-wave Luneburg lens in [21], for example, forms nine stable beams across the Ka-band with approximately $\pm 61^\circ$ angular coverage and peak gain up to 21.2 dB. Multi-feed Luneburg lenses have also provided up to 120° coverage in cellular base-station applications [22], while additively manufactured metamaterial-based implementations have achieved approximately $\pm 72^\circ$ beam coverage over 2–8 GHz with gain levels of 15.3–22 dB [23]. These representative implementations employ dedicated radiators designed for lens excitation and positioned at or near the intended focal surface, allowing the classical Luneburg feed-to-beam mapping to be preserved effectively.

The present work addresses a different integration problem in which five packaged commercial FMCW radar modules operate through a single shared passive aperture. Their finite package dimensions, fixed antenna locations and phase centers, module-to-lens clearance, and bistatic transmit/receive geometry constrain the available feed configuration. A conventional Luneburg lens can still produce a well-formed response for an individually excited radar feed; however, under a defined simultaneous multiport excitation condition, its purely radial phase profile provides no additional non-radial degrees of freedom for organizing the resulting shared-aperture response into prescribed sensing sectors. The proposed tailored Luneburg lens (TLL) therefore introduces a fabrication-aware non-radial GRIN distribution to control the optical-path and phase response of the radar-fed fields while retaining passive aperture enhancement. Adjacent-port coupling represents a related but distinct multi-radar effect and is evaluated separately in Section III.

Earlier radar-integrated GRIN lens studies have shown that even a single compact radar module can depart from ideal Luneburg excitation because of finite package dimensions, fixed antenna locations and phase centers, module-to-lens clearance, and bistatic or quasi-bistatic transmit/receive geometry [24, 25, 26]. The present work extends this practical integration problem to simultaneous multi-radar operation, where the shared aperture must support five spatially distinguishable sensing sectors under the mechanically constrained commercial-radar geometry. Luneburg lenses themselves are not new to radar or sensing; rather, to the best of the authors' knowledge, the specific gap addressed here is the absence of a commercial-radar-fed Luneburg lens employing a tailored non-radial GRIN profile for predefined multi-radar sector allocation. The combination of multiple commercial FMCW radar-module feeds, a shared passive aperture, fabrication-aware non-radial GRIN phase control, and sector-selective experimental validation constitutes the core contribution of this work.

At 60 GHz, the free-space wavelength is approximately 5 mm, so millimeter-scale feed offsets, placement errors, and fabrication tolerances can produce appreciable phase and beam-pointing deviations. In addition, the continuous GRIN permittivity profile must be approximated using discretized material distributions or effective-medium unit cells subject to fabrication limits on feature size, unit-cell period, material loss, and achievable effective permittivity. The radar geometry and fabrication constraints must therefore be considered jointly rather than treating the mm-wave lens as a direct scaled implementation of the ideal Luneburg profile.

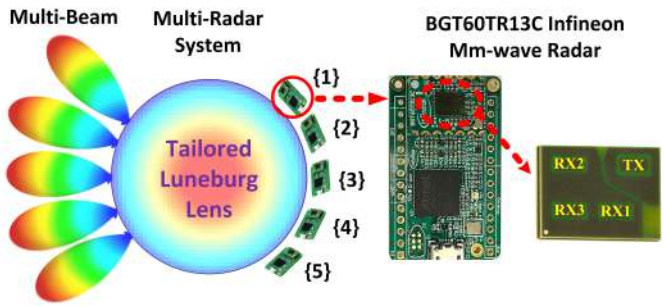


Figure 1: Concept of the proposed multi-beam GRIN Luneburg lens antenna fed by five Infineon BGT60TR13C mm-wave radar modules, generating simultaneous fixed beams for sectorized radar sensing.

The proposed passive multi-beam TLL, illustrated in Fig. 1, is a 10-cm-diameter spherical GRIN aperture integrated with five 58–63 GHz Infineon BGT60TR13C radar modules associated with sector centers at -56°, -28°, 0°, $+28^\circ$, and $+56^\circ$, providing approximately 140° of sectorized angular coverage. Under the defined five-port simulation condition, the TLL forms five dominant lobes near the prescribed directions with peak realized gains of approximately 20–22 dB, whereas the corresponding conventional Luneburg lens (CLL) response exhibits substantial central crowding and displaced sector maxima. The fabricated system is subsequently evaluated through received-power enhancement and simultaneous five-radar sector-selective detection.

An earlier version of this work was presented at EuCAP 2026 [27], introducing the multi-radar GRIN Luneburg lens concept, the 10-cm architecture, the rod-based tailored permittivity profile, and initial realized-gain results. The present article extends that work through a systematic TLL–CLL comparison under defined multiport excitation, a more complete fabrication-aware design analysis, adjacent-channel coupling characterization, and experimental validation using the fabricated five-radar prototype. The expanded measurements include received-power enhancement across the 58–63 GHz operating band and simultaneous sector-selective multi-radar detection.

The remainder of this paper is organized as follows. Section II presents the CLL baseline, the radar-fed TLL design, and its fabrication-aware implementation. Section III presents the full-wave comparison, sector-allocation analysis, frequency-dependent behavior, and adjacent-channel coupling. Section IV reports the received-power enhancement and sector-selective system-level measurements, and Section V concludes the paper.

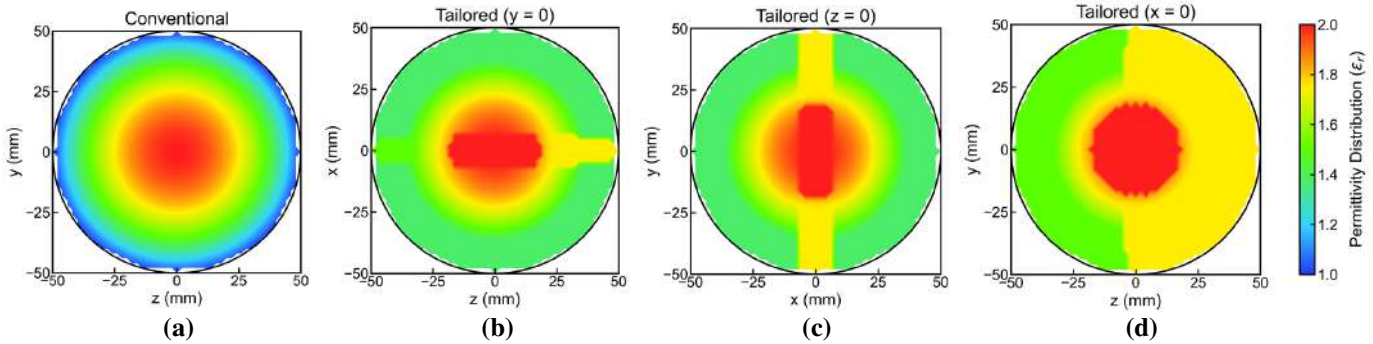


Figure 2: Permittivity distribution of the GRIN Luneburg lens structures: (a) Conventional spherical GRIN Luneburg lens, and tailored multi-beam TLL cross sections at (b) $y = 0$, (c) $z = 0$, and (d) $x = 0$, illustrating the localized dielectric tailoring introduced for radar-fed multi-beam aperture formation.

2. Multi-Beam GRIN Luneburg Lens Design for Millimeter-Wave Radar Integration

The proposed architecture uses a passive shared GRIN aperture simultaneously excited by five compact radar modules, each associated with a predefined sensing sector. The conventional Luneburg lens (CLL) serves as the reference because its spherical radial index profile provides the classical feed-to-beam mapping and therefore establishes a natural baseline for evaluating the proposed non-radial tailoring under the same five-radar geometry and simultaneous multiport excitation.

For a nonmagnetic dielectric medium, the refractive index and relative permittivity are related by $n(r) = \sqrt{\varepsilon_r(r)}$, where r is the radial distance from the lens center. The ideal CLL permittivity profile, shown in Fig. 2(a), is

$$\varepsilon_r^{\mathrm{CLL}}(r) = 2 - \left(\frac{r}{R}\right)^2, \qquad 0 \le r \le R, \tag{1}$$

where R is the lens radius. Outside the spherical volume, the surrounding medium is treated as free space.

Although the CLL provides effective feed-to-beam mapping under appropriate focal excitation, the packaged commercial-radar geometry and intended simultaneous five-port operation motivate additional control of the shared-aperture response. The proposed TLL retains the global GRIN behavior of the CLL while introducing non-radial dielectric tailoring to organize the multiport aperture response into the prescribed sensing sectors and reduce inter-sector overlap. Adjacent-port mutual coupling is a related but distinct effect and is quantified separately in Section III. The resulting structure operates as a passive simultaneous multi-beam aperture without mechanical scanning, phase shifters, or active beamforming.

2.1. Radar-Fed Multi-Beam Tailored Luneburg Lens Configuration

The TLL is designed to control the shared-aperture response under simultaneous multi-radar excitation. In a CLL, the purely radial refractive-index profile, $n_{\mathrm{CLL}}(r) = \sqrt{\varepsilon_r^{\mathrm{CLL}}(r)}$, provides the classical feed-to-beam mapping under appropriate focal excitation. In the present system, however, the packaged commercial FMCW radar modules impose fixed antenna locations and phase centers, finite package dimensions, module-to-lens clearance, and bistatic TX/RX geometry that constrain the practical feed configuration. Under the defined simultaneous five-port excitation condition, the field contributions from the five radar-fed responses superimpose through the common aperture. Because the CLL provides only its radial phase transformation, it offers no additional non-radial phase-control degrees of freedom to organize the resulting multiport field distribution. The TLL introduces this additional freedom to organize the multiport response around the prescribed sensing directions.

The radar front end is based on the Infineon BGT60TR13C mm-wave radar module. Because of the finite package dimensions and required physical clearance, arranging five modules around a common spherical lens imposes a minimum feasible adjacent-feed separation of approximately 28°. The modules are therefore positioned at sector centers of $-56°$, $-28°$, $0°$, $+28°$, and $+56°$, with all five operating simultaneously as independent transmit/receive sensing channels. Treating each channel as a nominal 28° sensing sector gives approximately 140° of sectorized angular coverage, extending from approximately $-70°$ to $+70°$, while the beam-center span extends from $-56°$ to $+56°$.

For radar sensing, sector allocation is critical because the useful received signal depends on the transmit and receive gains in the target direction. With transmitted power, wavelength, target radar cross section, and path length held fixed, the received signal level associated with the i-th sensing sector scales as

$$P_{\mathrm{RX},i} \propto G_{\mathrm{TX},i}(\theta_i) G_{\mathrm{RX},i}(\theta_i). \tag{2}$$

Accordingly, under the defined simultaneous five-port excitation condition, the multiport aperture response must maintain sufficient gain around each prescribed sector direction θ_i while limiting overlap with neighboring sectors. If the response maxima are displaced or crowded toward other angular regions, the useful illumination and collection gain in the intended sector are reduced even when the overall peak realized gain remains high. The TLL therefore modifies the phase response of the radar-fed fields so that the resulting multiport response forms dominant high-gain lobes near the five prescribed sensing directions, improving both the useful radar link and sector separation.

As reported in [24], compact single-radar CLL integration can exhibit TX/RX beam deviation because the transmit and receive phase centers of a bistatic radar module are spatially

separated. This offset can reduce the useful TX/RX gain overlap in the intended sensing direction and remains present in the TLL because dielectric tailoring does not remove the physical phase-center separation. In the present multi-radar system, the TLL must additionally organize the multiport aperture response under the defined simultaneous five-port excitation condition. Adjacent-port mutual coupling is treated separately in Section III.

In the present multi-radar configuration, the lens is electrically large relative to the TX/RX separation of an individual module. The selected design uses a lens diameter of $D = 2R =$ 100 mm, corresponding to approximately $20\lambda_0$ at 60 GHz. Denoting the effective TX/RX separation by d_{TR}, the angular offset of each phase center relative to the lens center is approximately

$$\theta_{\mathrm{TR}} \approx \tan^{-1}\left(\frac{d_{\mathrm{TR}}/2}{R}\right). \tag{3}$$

For $d_{\mathrm{TR}} \approx \lambda_0/2 = 2.5$ mm and $R = 50$ mm, this offset is approximately $\theta_{\mathrm{TR}} \approx 1.4^\circ$, substantially smaller than the 28° inter-sector spacing. Thus, although the TX/RX phase-center separation remains a relevant single-module nonideality, it is not the dominant source of the large sector displacement observed in the CLL response under the defined simultaneous five-port excitation condition. The dominant limitation in this case is the multiport field distribution produced by the five radar feeds, whose superposition through the radial CLL aperture leads to displaced maxima and central crowding.

A generalized Luneburg lens with a displaced focal point can compensate for a prescribed displacement of a feed from the ideal focal surface and therefore represents a viable approach when such focal displacement is the dominant limitation. In the present configuration, however, this represents only one component of the practical radar-feed geometry. The five packaged radar modules impose fixed antenna locations and phase centers, finite package dimensions, module-to-lens clearance, and bistatic TX/RX geometry while simultaneously exciting the same shared aperture. Moreover, the estimated angular separation associated specifically with the TX/RX phase-center offset of an individual module is only approximately 1.4°, substantially smaller than the observed sector-allocation errors and the 28° inter-sector spacing. Thus, the bistatic TX/RX separation alone cannot account for the large CLL sector displacement. The proposed TLL instead introduces non-radial volumetric phase-control degrees of freedom to organize the shared-aperture response of the complete five-feed configuration while retaining the underlying Luneburg-type GRIN behavior.

This limitation motivates a lens profile that preserves the passive aperture-enhancement capability of the Luneburg geometry while adding non-radial phase control for simultaneous multiport operation. The TLL therefore augments the radial CLL background with a radar-geometry-dependent GRIN distribution that modifies the optical paths and phase response of the radar-fed fields. The tailored regions do not form isolated dielectric channels; fields from the different radar feeds propagate through and overlap within the same shared lens volume. The phase accumulated along a dominant propagation path Γ_i associated with the i-th radar feed is

$$\Phi_i = k_0 \int_{\Gamma_i} n(\mathbf{r})\, ds = k_0 \int_{\Gamma_i} \sqrt{\varepsilon_r(\mathbf{r})}\, ds, \tag{4}$$

where $k_0 = 2\pi/\lambda_0$, $n(\mathbf{r})$ is the local refractive index, and ds is the differential path length. Equation (4) shows that modifying the local permittivity changes the optical path length and accumulated phase. Because the five radar feeds illuminate the same non-radial distribution from different angular positions, the tailored profile introduces feed-dependent phase corrections that modify their field contributions under the defined multiport excitation condition, thereby organizing the resulting multiport aperture response around the prescribed sensing sectors.

For the present implementation, the prescribed sector-center angles in the elevation plane are

$$\theta_i = -56^\circ, -28^\circ, 0^\circ, +28^\circ, +56^\circ, \qquad i = 1, \ldots, 5. \tag{5}$$

The sector centers are separated by $\Delta\theta \approx 28^\circ$. Treating each channel as a nominal 28° sensing sector gives an overall sectorized coverage of $\Theta_{\mathrm{cov}} \approx 5\Delta\theta \approx 140^\circ$, extending approximately from -70° to $+70^\circ$, while the beam-center span extends from -56° to $+56^\circ$.

The desired beam direction for the i-th radar channel is defined by the unit vector

$$\mathbf{v}_i = \begin{bmatrix} 0 \\ \sin\theta_i \\ \cos\theta_i \end{bmatrix}, \qquad i = 1, \ldots, N, \tag{6}$$

with $N = 5$ in the present implementation. For an ideally phase-corrected aperture, the local phase gradient associated with each radar-fed field contribution should satisfy $\nabla\Phi_i(\mathbf{r}) \parallel \mathbf{v}_i$. The tailored GRIN profile modifies these phase contributions so that, under the defined simultaneous five-port excitation condition, the resulting multiport response forms dominant lobes near the prescribed sensing directions.

The implemented TLL distribution combines a fabrication-bounded GRIN background with rotated instances of a single canonical dielectric tailoring rod,

$$\varepsilon_r^{\mathrm{TLL}}(\mathbf{r}) = \max\left[\varepsilon_r^{\mathrm{base}}(\mathbf{r}), \psi_1(\mathbf{r}), \psi_2(\mathbf{r}), \ldots, \psi_{N_{\mathrm{rot}}}(\mathbf{r})\right], \tag{7}$$

where $\varepsilon_r^{\mathrm{base}}(\mathbf{r})$ is the bounded Luneburg-type background profile and $\psi_j(\mathbf{r})$ denotes the j-th rotated instance of the canonical tailoring rod. The parameter N_{rot} defines the number of angular orientations used to distribute the rod across the aperture. The maximum operation preserves the GRIN background where it dominates and introduces additional dielectric loading only where the tailoring function exceeds the background value. The resulting profile retains the global Luneburg-type focusing behavior while adding the non-radial phase-control degrees of freedom required to organize the multiport response under the defined five-port excitation condition.

The implemented non-radial perturbation uses a single canonical three-section dielectric rod rotated through multiple angular orientations within the shared aperture. The five radar modules define the $N = 5$ prescribed sector directions, while the rotated rod instances provide the spatial distribution required

to control the multiport aperture response. The number of rod orientations used to generate the permittivity map is denoted by N_{rot}. The fabrication-bounded background profile is

$$\varepsilon_r^{\mathrm{base}}(x,y,z) = 0.8 + 1.2\left[1 - \frac{x^2+y^2+z^2}{R^2}\right], \tag{8}$$

subject to the lower-bound constraint

$$\varepsilon_r^{\mathrm{base}}(x,y,z) \leftarrow \max\left[\varepsilon_r^{\mathrm{base}}(x,y,z), 1.38\right]. \tag{9}$$

This bounded profile retains the radial GRIN variation of the Luneburg lens while restricting the permittivity range to values compatible with the selected fabrication process. It reaches $\varepsilon_r = 2.0$ at the lens center, matching the ideal Luneburg core, while the lower-bound constraint enforces a minimum effective permittivity of $\varepsilon_r = 1.38$. Consequently, the implemented profile departs from the ideal Luneburg distribution near the outer boundary, where ε_r would approach unity. The resulting $\varepsilon_r \approx 1.38$ boundary introduces a residual impedance mismatch with air and a corresponding reflection penalty relative to the ideal profile.

Within the fabrication-bounded GRIN background, the non-radial tailoring is implemented as a volumetric phase-shaping structure formed by rotating the canonical dielectric rod through multiple angular orientations across the shared aperture. The rotated instances do not represent additional feeds, beams, or isolated dielectric channels; their overlap instead forms a continuous three-region volume comprising a central high-permittivity region and two outer regions with lower dielectric loading. This structure modifies the optical path lengths associated with the radar-fed fields so that they acquire the phase corrections required to produce the prescribed sectorized response under the defined multiport excitation condition.

The angular tailoring directions used to generate this volumetric distribution are

$$\hat{\mathbf{u}}_j = \begin{bmatrix} 0 \\ \sin\alpha_j \\ \cos\alpha_j \end{bmatrix}, \qquad \alpha_j \in [-85^\circ, 85^\circ], \qquad j = 1,\ldots,N\mathrm{rot}, \tag{10}$$

where $N_{\mathrm{rot}} = 12$ in the implemented design. All 12 rod instances have identical transverse dimensions and three-section axial geometry, differing only in their angular orientations α_j, which span the elevation plane over $[-85^\circ, 85^\circ]$. Their overlap covers the required angular extent of the shared aperture and forms a continuous tailored volume rather than independent dielectric channels. For an arbitrary point $\mathbf{r} = (x,y,z)$ inside the lens, the axial coordinate along the j-th orientation is $s_j = \mathbf{r}\cdot\hat{\mathbf{u}}j$, and the corresponding transverse distance is $r\perp, j = \left|\mathbf{r} - s_j\hat{\mathbf{u}}j\right|$. A point belongs to the j-th rod instance when $r\perp, j < a$, where $a = 7.5$ mm defines the transverse radius of the tailoring region. For $R = 50$ mm, s_j spans approximately -50 mm to $+50$ mm and is divided into radar-facing, central, and radiation-facing sections over $-50 \le s_j \le -17$ mm, $-17 < s_j \le 17$ mm, and $17 < s_j \le 50$ mm, respectively. The corresponding permittivities are $\varepsilon_1 = 1.5$, $\varepsilon_2 = 2.0$, and $\varepsilon_3 = 1.75$. These dielectric-loading values originate from the optical-path and phase formulation established in [24], but their direct implementation at 60 GHz is constrained by the realizable effective-permittivity range and spatial resolution of the mm-wave gyroid fabrication process. The phase-loading requirements were therefore refined through a fabrication-constrained design trade-off to preserve the required differential phase correction within the realizable permittivity range. Combined with the bounded GRIN background, the overlapping rod instances form the continuous high-permittivity central region and asymmetric outer dielectric-loading regions shown in Fig. 2(b)–(d).

The implemented tailoring function for each angular direction is therefore

$$\psi_j(\mathbf{r}) = \begin{cases} 1.5, & r_{\perp,j} < a, \quad -50 \le s_j \le -17, \\ 2.0, & r_{\perp,j} < a, \quad -17 < s_j \le 17, \\ 1.75, & r_{\perp,j} < a, \quad 17 < s_j \le 50, \\ 0, & \text{otherwise}, \end{cases} \tag{11}$$

with s_j expressed in millimeters. Combined with the bounded GRIN background through the maximum operation of Eq. (7), this piecewise loading produces the volumetric profile shown in Fig. 2(b)–(d), comprising a high-permittivity central region and two asymmetrically loaded outer regions. The central section, with $\varepsilon_r = 2.0$, provides the highest absolute dielectric loading, while the radar-facing section, with $\varepsilon_r = 1.5$, shapes the initial phase accumulation of the feed-excited fields and provides a gradual transition into the bounded GRIN background.

On the radiation-facing side, the tailoring region controls the outgoing phase before the field exits the lens. The selected value $\varepsilon_r = 1.75$ therefore serves as a final phase-loading section rather than a free-space matching layer. Because $\varepsilon_r > 1$, a residual impedance mismatch remains at the lens–air boundary; however, reducing this value toward unity would weaken the optical-path correction required to organize the multiport aperture response under the defined excitation condition. The radiation-facing section therefore represents a trade-off between output phase control and boundary reflection.

The phase loading introduced by the tailored profile can be estimated from the optical-path difference between the implemented TLL and the bounded GRIN background. For the three axial sections, the added phase is

$$\Delta\Phi_m \approx k_0 \int_{s_m} \left[\sqrt{\max\left(\varepsilon_r^{\mathrm{base}}(s), \varepsilon_m\right)} - \sqrt{\varepsilon_r^{\mathrm{base}}(s)}\right] ds, \tag{12}$$

where $m = 1,2,3$ denotes the radar-facing, central, and radiation-facing sections, with $\varepsilon_1 = 1.5$, $\varepsilon_2 = 2.0$, and $\varepsilon_3 = 1.75$, respectively. At $f_0 = 60$ GHz, $k_0 \approx 1.257$ rad/mm, and the section lengths are $L_1 = 33$ mm, $L_2 = 34$ mm, and $L_3 = 33$ mm over the intervals $[-50,-17]$, $[-17,17]$, and $[17,50]$ mm. Evaluating Eq. (12) gives $\Delta\Phi_1 \approx 0.996$ rad (57.1°), $\Delta\Phi_2 \approx 0.706$ rad (40.5°), and $\Delta\Phi_3 \approx 3.724$ rad (213.4°), for a total added phase of approximately 5.43 rad (311°) along the centerline. The asymmetric contributions arise from the local refractive-index contrast between the tailored and background profiles. Although the central section has the highest absolute permittivity, the radiation-facing section produces the largest differential phase because the bounded GRIN background

approaches its lower-permittivity limit in this region. The three-section profile therefore provides a deliberately nonuniform optical-path correction across the shared aperture.

The final TLL permittivity distribution is sampled over x, y, and z from -50 mm to $+50$ mm with a 2 mm spatial step and imported directly into the full-wave solver. The CLL and TLL are evaluated using identical radar positions, simultaneous five-port excitation conditions, aperture dimensions, frequency settings, and simulation boundaries. This controlled comparison isolates the effect of the tailored permittivity distribution on the resulting multiport radiation response while retaining the same commercial-radar geometry, material loss, finite feed aperture, diffraction, and shared-aperture environment.

2.2. Fabrication-Aware Implementation of the TLL

At millimeter-wave frequencies, the tailored GRIN profile must satisfy practical fabrication constraints. An ideal Luneburg lens assumes a continuously varying permittivity, whereas the physical implementation approximates this distribution using discrete effective-medium unit cells. Following the fabrication approach of [24], the GRIN structure is realized using gyroid unit cells printed in Rogers Radix$^{\text{TM}}$ dielectric resin, with relative permittivity $\varepsilon_{r,\text{resin}} = 2.8$ and loss tangent $\tan\delta = 0.0043$ specified at 10 GHz. The local effective permittivity is controlled through the air fraction of each unit cell, enabling the required GRIN distribution using a single printable dielectric material.

The spatial discretization must remain sufficiently small relative to the wavelength for the printed lattice to approximate an effective medium. Denoting the unit-cell period by Δ, the relevant normalized scale is Δ/λ_d, where $\lambda_d = \lambda_0/\sqrt{\varepsilon_{\text{eff}}}$. For the maximum assigned permittivity, $\varepsilon_{\text{eff}} = 2.0$, a fine unit-cell period of $\Delta = 0.5$ mm gives $\Delta/\lambda_d = 0.14$, providing a substantially finer effective-medium approximation but imposing more demanding fabrication requirements over the full three-dimensional lens volume. The manufacturable period adopted for the implemented TLL, $\Delta = 2$ mm, gives $\Delta/\lambda_d = 0.57$ and therefore represents a coarser approximation. This comparison illustrates the trade-off between effective-medium fidelity and practical mm-wave fabrication resolution and explains why spatial discretization is substantially more restrictive than in the X-band implementation of [24].

The 10-cm lens diameter is dictated by both the physical arrangement of the five radar modules and the fabrication requirements of the tailored GRIN distribution. For a manufacturable unit-cell period of $\Delta = 2$ mm and $R = 50$ mm, the number of radial sampling intervals is approximately $N_R \approx R/\Delta = 25$, providing sufficient spatial degrees of freedom to approximate the bounded GRIN background and local tailored regions. A larger radius also increases the available optical-path length over which the dielectric loading accumulates phase, thereby reducing the permittivity contrast required for the prescribed phase correction. Conversely, reducing the lens size while retaining the same radar packages and fabrication resolution would decrease both the available spatial sampling and phase-accumulation length, requiring stronger dielectric loading that may exceed the realizable permittivity range of the selected mm-wave fabrication process.

The achievable effective-permittivity range is likewise constrained by the unit-cell geometry and fabrication process. In [24], an initial high-permittivity rod design required values up to $\varepsilon_r = 3.4$, exceeding the practical range of the selected 3D-printing process; a fabrication-aware redesign using overlapping rod regions reduced the required range to approximately $1.15 < \varepsilon_r < 2.4$ at X-band. The present 60 GHz TLL follows the same principle under stricter mm-wave fabrication constraints. The selected values $\varepsilon_r = 1.5$, 1.75, and 2.0 remain within the practical range of the printed gyroid implementation, with $\varepsilon_r \approx 2$ representing the upper realizable limit. Together with the longer optical path provided by the 100-mm aperture, this permittivity range enables the required nonuniform phase loading without demanding dielectric values beyond the fabrication capability.

The final design therefore balances aperture size, radar-feed spacing, unit-cell resolution, achievable permittivity contrast, material loss, and fabrication tolerances. A larger radius provides the physical space required for the five radar modules, increases the available spatial sampling, and extends the optical path for phase correction, whereas a smaller radius improves compactness but reduces the number of effective radial layers and the available phase-accumulation length, increasing sensitivity to feed displacement, discretization, and the required dielectric contrast. Fabrication tolerances also affect performance; as reported in [24], permittivity variations above approximately 10–13% can reduce gain and shift the main beam, while unit-cell discretization introduces additional degradation. The selected 10-cm-diameter TLL therefore represents a deliberate compromise among commercial-radar packaging, multiport phase control, achievable permittivity contrast, spatial resolution, and fabrication feasibility at 60 GHz.

3. Full-Wave Validation and Multi-Beam Performance

The proposed TLL is evaluated through full-wave electromagnetic simulations across the 58–63 GHz operating band of the Infineon BGT60TR13C module, with the principal radiation-pattern comparison presented at 60 GHz. Two reference configurations are considered: the standalone radar module and the same five-radar system integrated with the CLL. The CLL and TLL cases use identical radar positions, simultaneous five-port excitation conditions, aperture dimensions, frequency settings, and simulation boundaries, while the standalone module provides the corresponding single-feed reference. The comparison focuses on multiport realized-gain response, sector allocation under simultaneous excitation, single-port versus five-port performance, and adjacent-channel coupling.

In the five-port full-wave simulations, all five radar ports are excited simultaneously with equal amplitudes and identical initial phases. This excitation is used as a deterministic reference state so that the CLL and TLL are compared under identical multiport conditions; it is not intended to imply RF carrier-phase locking among the five physical radar modules. In the experimental platform, the five BGT60TR13C modules operate simultaneously as independent FMCW sensing channels with temporally synchronized data acquisition and fusion. Accordingly, the simulations characterize the shared-aperture

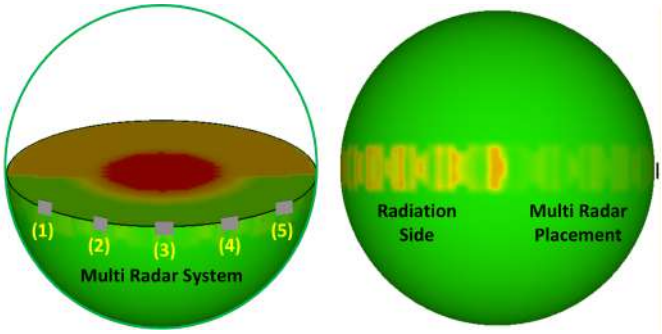


Figure 3: Simulated geometry of the five-radar TLL configuration. The left view shows the cross-sectional placement of radar modules (1)–(5) around the shared lens aperture. The right view shows an orthogonal view of the same configuration, identifying the radar-placement side and the opposite radiation side of the TLL.

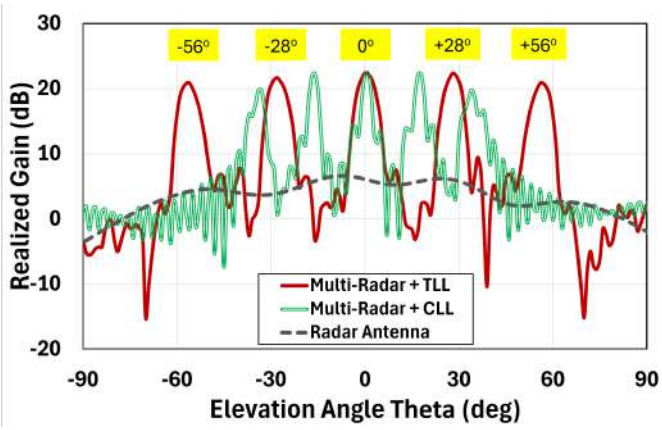


Figure 4: Simulated realized-gain patterns of the standalone radar and simultaneously excited five-radar CLL and TLL configurations at 60 GHz. The dashed curve denotes the standalone radar at $\theta = 0^\circ$.

electromagnetic response under a defined multiport excitation state, whereas the measurements in Section IV provide channel-resolved system-level validation of received-power enhancement and sector-selective sensing.

Figure 3 shows the simulated five-radar geometry used for the full-wave analysis. Radar modules (1)–(5) are distributed along the lower side of the shared lens aperture, with module (3) aligned with boresight and the remaining modules providing the off-axis excitations associated with the prescribed sensing sectors. In the multi-beam configuration, all five radar ports are excited simultaneously, allowing the effect of the tailored permittivity distribution on the multiport shared-aperture response to be evaluated.

Figure 4 compares the simulated realized-gain responses of the standalone radar antenna and the simultaneously excited five-radar configurations integrated with the CLL and TLL. The standalone radar exhibits a broad response with limited gain due to its compact embedded antenna aperture, while integration with either GRIN lens provides substantial aperture enhancement. The key distinction appears under simultaneous five-port excitation: although the CLL can provide well-formed responses for individually excited feeds, their superposition under the defined equal-amplitude, equal-phase five-port reference excitation produces displaced composite maxima, central crowding, and increased inter-sector overlap. The TLL modifies the phase response of the radar-fed field contributions so that the resulting multiport response is organized into five dominant high-gain lobes near the prescribed sensing directions.

For the simultaneously excited CLL configuration, the realized gain remains high, confirming the aperture-enhancement capability of the conventional Luneburg profile. However, under the defined five-port reference excitation, superposition of the five CLL-fed field contributions produces a composite response whose dominant maxima are not consistently aligned with the prescribed sector directions; several maxima crowd toward the central angular region, with additional lobes appearing between adjacent sectors. Thus, although the radial CLL profile effectively focuses the individual feed responses, it provides no additional non-radial phase-control degrees of freedom to organize their simultaneous composite radiation pattern. The CLL therefore preserves high gain but exhibits substantial sector-allocation error, central crowding, and reduced inter-sector separation under five-port excitation.

The proposed TLL, under the same simultaneous five-port excitation, produces five dominant high-gain lobes closely aligned with the prescribed directions of -56°, -28°, 0°, $+28^\circ$, and $+56^\circ$, while maintaining peak realized gains of approximately 20–22 dB. The tailored non-radial permittivity distribution therefore preserves the aperture-enhancement benefit of the Luneburg lens while modifying the phase response of the radar-fed field contributions so that the resulting multiport response is organized around the intended sensing sectors.

The improvement is most pronounced in the outer sectors. In the simultaneous five-port CLL response, the dominant maxima associated with the prescribed $\pm 56^\circ$ sectors occur at approximately $\pm 27^\circ$–$\pm 30^\circ$, corresponding to angular allocation errors of approximately 26°–29°. The TLL relocates these composite maxima to approximately $\pm 54^\circ$, reducing the error to about 2°. A similar improvement is observed for the intermediate sectors: the CLL composite maxima associated with the prescribed $\pm 28^\circ$ sectors occur near $\pm 9^\circ$–$\pm 10^\circ$, corresponding to errors of approximately 18°–19°, whereas the TLL places the corresponding maxima close to the prescribed $\pm 28^\circ$ directions.

The principal advantage of the TLL is therefore not higher peak realized gain, but controlled organization of the simultaneous multiport aperture response around the prescribed sensing sectors. Relative to the CLL, the TLL substantially improves sector-allocation accuracy and inter-sector separation while reducing central crowding and unintended radiation between sectors. These results demonstrate that the tailored GRIN distribution enables the shared aperture to operate as a passive simultaneous multi-beam front end for sectorized millimeter-wave radar sensing.

The conventional peak aperture efficiency of the 100-mm-diameter lens can be estimated as $(G_{\max}\lambda_0^2)/(4\pi A_{\text{phys}})$, where $A_{\text{phys}} = \pi R^2$. For the present configuration, using the maximum simulated realized gain of approximately 22 dBi, this

corresponds to a peak aperture efficiency of approximately 4% at 60 GHz. This metric should be interpreted in the context of the system-constrained architecture rather than as the efficiency of a conventional Luneburg aperture optimized around a dedicated focal feed. In particular, the physical dimensions and required clearance of the five packaged commercial radar modules impose a minimum feasible adjacent-feed separation of approximately 28°, directly constraining the lens diameter and five-radar aperture geometry.

The relatively low conventional efficiency is not an inherent limitation of Luneburg lenses at millimeter-wave frequencies. A conventional Luneburg lens excited by a suitably designed focal feed can achieve high aperture efficiency; however, the commercial radar modules considered here impose fixed antenna locations and phase centers, bistatic TX/RX geometry, radiation characteristics, and module-to-lens clearance. Correcting the resulting nonideal excitation also introduces a trade-off between absolute peak gain and gain delivered in the prescribed sensing direction. This behavior is illustrated by the separate 60-GHz single-radar TLL study in [26]. For a 50-mm-diameter lens, the CLL reaches approximately 24.8 dBi peak realized gain, but its TX and RX responses are tilted to approximately $\pm 6^\circ$, leaving only approximately 12 dB at the prescribed boresight direction. The tailored profile redirects both responses to $\theta = 0^\circ$ and provides approximately 20 dBi at boresight, corresponding to approximately 10% peak aperture efficiency by the same conventional definition. The reduced absolute peak therefore reflects the phase redistribution required to correct the commercial-radar-induced beam displacement and deliver the aperture-enhanced response in the required direction, rather than an intrinsic inefficiency of the Luneburg-lens principle.

The present five-radar implementation introduces additional mm-wave fabrication and integration constraints. At 60 GHz, the approximately 5-mm free-space wavelength makes the tailored phase response sensitive to millimeter-scale spatial discretization and fabrication tolerances. The manufacturable 2-mm unit-cell period provides a relatively coarse effective-medium approximation, while the realizable effective-permittivity range is restricted to approximately $1.38 \leq \varepsilon_r \leq 2.0$. In addition, reducing the aperture size would decrease both the number of spatial samples and the optical-path length available for phase accumulation, requiring stronger dielectric loading that may exceed this realizable range. By comparison, the computational single-radar design in [26] uses a finer 0.5-mm sampling step and dielectric tailoring values up to $\varepsilon_r = 2.4$. The 100-mm diameter of the present TLL therefore represents a compromise among the physical size of the five commercial radar modules, the required 28° feed spacing, phase-correction length, spatial resolution, realizable dielectric contrast, and fabrication feasibility. Higher aperture efficiency can be pursued through radar–lens co-design, smaller feed modules, lens-optimized radiators, finer fabrication resolution, lower-loss materials, and a larger dielectric-contrast range.

Figure 5 compares the frequency-dependent realized gain under single-port and simultaneous five-port excitation for the CLL and TLL across the 58–63 GHz band. Near the band center, transitioning to simultaneous five-port excitation reduces the CLL gain by approximately 2.6 dB, whereas the TLL exhibits

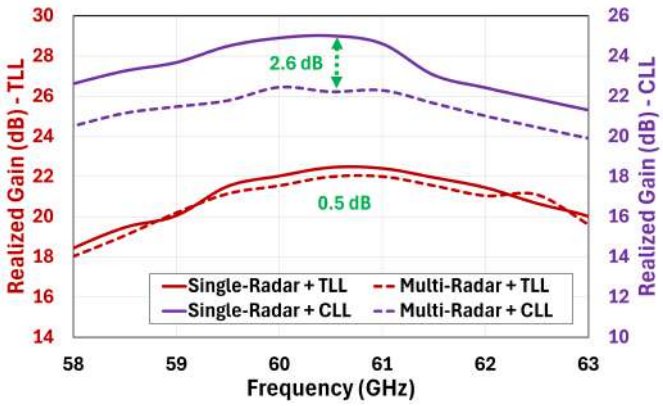


Figure 5: Simulated realized-gain variation of the CLL and TLL configurations under single-port and simultaneous five-port excitation across the 58–63 GHz operating band.

only about 0.5 dB reduction. This smaller degradation shows that the tailored permittivity distribution better preserves the aperture-enhanced response when the five radar-fed fields operate simultaneously, complementing the improved composite sector allocation demonstrated in Fig. 4.

The adjacent-channel interaction is quantified separately through the simulated transmission coefficient S_{ij} between neighboring radar channels for the radar-only, CLL-integrated, and TLL-integrated configurations, as shown in Fig. 6. The radar-only case exhibits a relatively flat coupling level of approximately -38 to -41 dB across the 59–61 GHz interval. Although this represents weak direct coupling relative to the transmitted power, radar detection relies on substantially weaker target echoes after two-way propagation and target scattering. Consequently, even relatively low inter-channel leakage can contribute to the interference observed by a neighboring radar receiver and should be considered relative to the desired reflected signal rather than to the transmitted power alone. Introducing the shared CLL modifies the electromagnetic field-transfer paths between neighboring radar locations, producing a more frequency-dependent S_{ij} response without consistently reducing the adjacent-channel transfer.

In addition to direct port-to-port leakage, sectorized multi-radar sensing is affected by the spatial overlap of the radar TX/RX responses. If neighboring responses overlap or are displaced from their prescribed directions, a target associated with one sector can also produce an undesired response in another radar channel, reducing channel selectivity and increasing cross-sector ambiguity. The TLL therefore addresses two complementary aspects of the multi-radar sensing problem: the angular organization of the TX/RX aperture response, demonstrated in Fig. 4, and the direct adjacent-channel field transfer quantified by S_{ij} in Fig. 6.

The TLL further modifies the shared-aperture field transfer and produces pronounced frequency-selective coupling suppression near the design frequency. Around 60 GHz, the adjacent-channel transmission coefficients reach approximately -50 to -70 dB, depending on the radar pair, compared with approximately -38 to -41 dB for the radar-only configuration. The

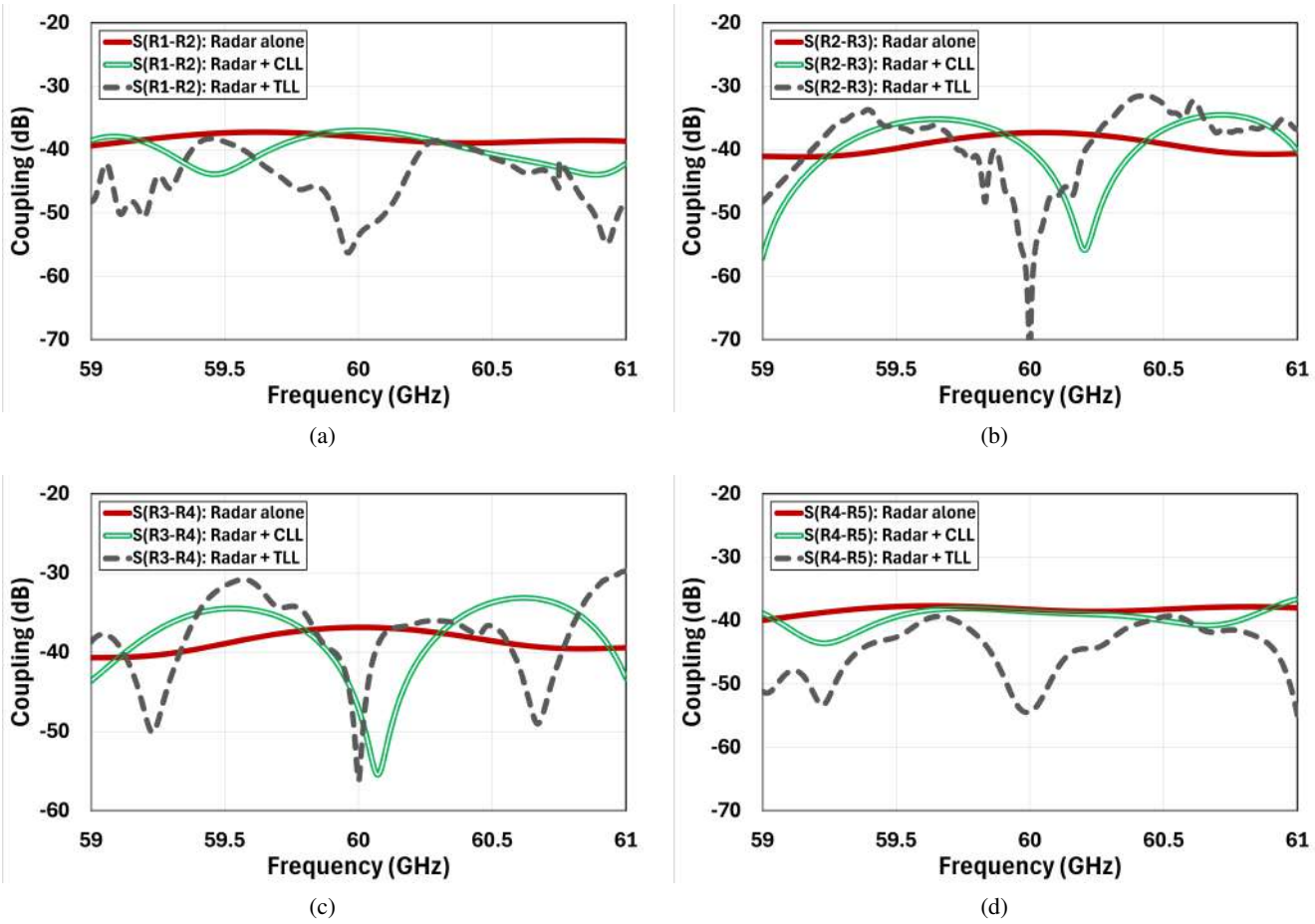


Figure 6: Simulated adjacent-channel transmission coefficients between neighboring radar modules for the radar-only, CLL-integrated, and TLL-integrated configurations over the 59–61 GHz region around the 60 GHz design frequency: (a) $S(R_1–R_2)$, (b) $S(R_2–R_3)$, (c) $S(R_3–R_4)$, and (d) $S(R_4–R_5)$.

significance of this additional suppression is not that a particular coupling value is required for operation, but that the TLL provides additional isolation between neighboring radar channels rather than introducing a coupling penalty through the shared aperture. Reduced adjacent-port transfer limits direct electromagnetic leakage into neighboring radar receivers, while the improved TX/RX sector alignment in Fig. 4 strengthens the desired two-way response in the prescribed sensing direction and reduces spatial overlap with adjacent sectors. Together, these complementary effects improve channel-specific received-signal quality and reduce cross-sector ambiguity or unintended channel activation.

This coupling reduction is frequency selective and is therefore interpreted as design-frequency adjacent-channel isolation rather than broadband decoupling. Near the 60 GHz design frequency, the frequency-dependent phase response of the tailored dielectric regions produces the pronounced coupling minima observed in Fig. 6. Away from this region, the coupling gradually approaches the levels of the radar-only and CLL-integrated configurations. Accordingly, Fig. 6 focuses on the 59–61 GHz region in which the strongest coupling suppression occurs. The isolation bandwidth of the TLL is narrower than the full 58–63 GHz FMCW sweep; however, this does not prevent the radar modules from operating across their complete modulation bandwidth for range estimation. Rather, the TLL provides its strongest inter-channel isolation around the design frequency while retaining the broader aperture-enhancement behavior demonstrated experimentally across the 58–63 GHz band. For the present sensing configuration, the frequency-selective isolation around 60 GHz provides additional suppression of adjacent-channel field transfer near the design frequency. Future work will focus on broadening this isolation bandwidth through multi-section dielectric loading, broadband phase-gradient optimization, and bandwidth-constrained inverse design of the tailored GRIN profile.

The validation results show that the TLL performs three complementary functions: it enlarges the effective aperture of the compact radar modules, organizes the simultaneous multi-port TX/RX response into five high-gain lobes aligned with the prescribed sensing sectors, and reduces adjacent-channel field transfer near the design frequency. Together, these functions improve the desired sector-specific radar response while reducing electromagnetic and spatial interference between neighboring sensing channels, and are achieved passively through the tailored GRIN distribution without mechanical scanning, phase shifters, or active beamforming.

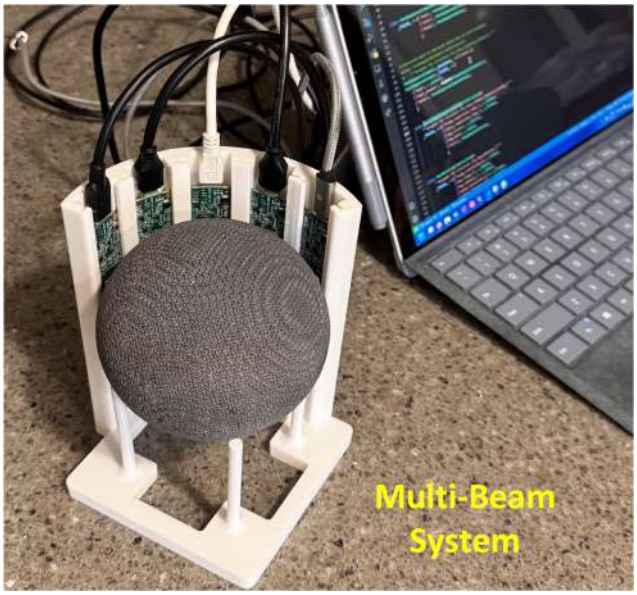


Figure 7: Fabricated prototype and measurement setup of the proposed multi-beam TLL system. The tailored GRIN Luneburg lens is integrated with five compact millimeter-wave radar modules using a custom holder that maintains their positions and orientations relative to the shared aperture.

4. Experimental System-Level Validation

Fig. 7 shows the fabricated TLL prototype and the experimental setup used for system-level validation. The tailored GRIN Luneburg lens is mounted in a custom 3D-printed holder with five compact millimeter-wave radar modules positioned along the lower side of the shared aperture. The fixture maintains the relative positions and orientations of the five modules with respect to the lens, providing a repeatable geometry for the measurements.

For the received-power measurements, a standard millimeter-wave horn antenna connected to a spectrum analyzer was positioned in front of the radar system. All five radar modules were operated simultaneously, consistent with the intended multi-radar configuration, while the received power corresponding to one selected radar TX antenna was recorded at the horn. Identical alignment and instrument settings were maintained for the standalone-radar and TLL-integrated configurations.

The experimental validation was performed at the system level because the platform uses integrated FMCW radar modules rather than connectorized standalone antennas. The TLL was therefore evaluated through two radar-relevant measurements: received-power enhancement across the operating band and sector-selective detection using the TLL-integrated multi-radar configuration. For the received-power measurement, identical geometry, alignment, and instrument settings were maintained for the standalone-radar and TLL-integrated cases so that the measured difference represents the relative enhancement introduced by the lens. Together, these measurements assess the two principal system-level functions of the TLL: aperture-enhanced power delivery and spatially selective sensing.

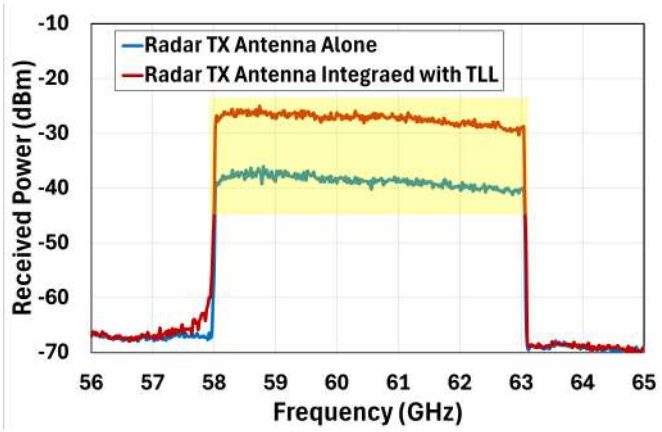


Figure 8: Measured received power at the reference horn for one selected radar TX antenna with and without the proposed TLL. The TLL-integrated configuration provides approximately 10–13 dB received-power enhancement across the 58–63 GHz operating band, confirming the broadband aperture-enhancement effect of the fabricated lens.

Fig. 8 shows the received power measured at the reference horn for the standalone radar TX antenna and the TLL-integrated configuration across the 58–63 GHz operating band. The standalone radar produces approximately -38 to -41 dBm, whereas the TLL-integrated configuration increases the received power to approximately -26 to -30 dBm, corresponding to an enhancement of approximately 10–13 dB across the band. This measured enhancement is consistent in magnitude with the approximately 13-dB peak aperture enhancement predicted by simulation. The comparison should be made with the corresponding standalone-radar peak reference for the selected radar orientation, rather than with the value of the unrotated standalone pattern at the corresponding off-axis sector angle. The remaining difference between simulation and measurement is expected because Fig. 4 reports peak simulated realized gain, whereas Fig. 8 reports system-level received power at a fixed measurement geometry using the fabricated radar–lens assembly.

The measured 10–13 dB enhancement confirms that the TLL increases the effective aperture of the compact radar antenna and improves power delivery toward the receiving direction across nearly the full 58–63 GHz band. This measurement is not intended as a calibrated antenna-gain measurement; rather, it provides a system-level comparison under identical radar settings, receiving geometry, alignment, and instrument configuration. Because the radar antenna, module package, and lens operate as an integrated sensing front end, the measured received-power increase directly validates the practical aperture-enhancement benefit of the TLL while demonstrating compatibility with the FMCW operating bandwidth.

Fig. 9 evaluates the sector-selective operation of the fabricated TLL-integrated multi-radar system using a corner reflector as a controlled target. During this experiment, all five synchronized radar channels operated simultaneously, and their detection outputs were evaluated in parallel. The detection output is shown for the no-object condition and for the reflector



Figure 9: Experimental system-level sector-selective detection using the fabricated TLL-integrated five-radar system under simultaneous operation. A corner reflector is placed sequentially in the five prescribed sensing sectors. Under the selected detection threshold, the no-object condition produces no activation, while a target in each tested sector activates the corresponding radar channel and the remaining channels stay below the threshold.

placed sequentially in each of the five prescribed sensing sectors. Under the selected detection threshold, no radar channel is activated in the absence of the reflector. When the reflector is placed in a given sector, the corresponding radar channel exceeds the detection threshold, while the remaining channels remain below it for the tested target positions.

This measurement provides system-level experimental validation of sector-selective operation in the simultaneous five-radar configuration and complements the full-wave angular analysis in Fig. 4. Whereas Fig. 4 characterizes the simulated shared-aperture response under the defined multiport excitation condition, Fig. 9 evaluates the end-to-end sensing behavior of the fabricated system with all five radar channels operating simultaneously. For the tested target positions, the radar channel associated with the reflector sector is selectively activated while the remaining channels stay below the detection thresh-

Table 1: Comparison of This Work with Representative Radar-Integrated Aperture and Lens Enhancement Methods

Ref	Freq.	Aperture Type	Feed Configuration	Beam Mode	Primary Advancement & Key Architectural Limitation
[28]	77 GHz	Thin dielectric lens	2×2 patch-array feeder	Single beam	High-gain lens for automotive radar; limited to a single-beam architecture without multi-radar shared-aperture sector allocation.
[29]	77 GHz	PCB metamaterial, Fresnel-type lens	Commercial MMIC monostatic/bistatic	Single beam	Thin lens implementation for radar front ends; does not provide tailored sector allocation for multiple radar modules sharing one aperture.
[30]	77 GHz	Metasurface folded transmitarray	SIW slot-feed radar antenna	Single beam	Low-profile folded transmitarray for radar gain enhancement; restricted to a single feed rather than a shared multi-feed volumetric aperture.
[31]	60/77 GHz	Dual-band Huygens metasurface lens	Automotive mm-wave radar antenna	Dual-band	Orthogonally polarized dual-band operation; does not address multi-radar sectorized sensing or feed-dependent non-radial phase correction.
[32]	mm-wave	Metamaterial surface inside radome layer	Signal-sensing radar array antenna	Single beam	Reduces radome-related transmission loss; does not provide multi-beam sector allocation through a shared passive aperture.
[3]	58–63 GHz	Planar near-field metasurface	Single compact mm-wave radar module	Focused zone	Enhances localized near-field power concentration; restricted to single-radar operation without multi-sector beam allocation.
[24]	X-band	Tailored dielectric GRIN Luneburg lens	Single radar / antenna configuration	Single beam	Enhances radar sensing and corrects nonideal single-feed excitation; restricted to single-radar operation without multi-feed shared-aperture sectorization.
[26]	60 GHz	Computational tailored GRIN Luneburg lens	Single commercial bistatic radar module	Single beam	Corrects commercial-radar TX/RX beam tilting and aligns both responses to boresight; limited to a single-radar computational configuration without shared-aperture multi-sector operation.
[33]	Micro/ mm-wave	Space-time-coding metasurface aperture	Metasurface-based TX/RX architecture	Dynamic	Enables dynamic waveform and aperture control; relies on active space-time coding rather than a passive fixed multi-beam add-on.
[34]	60 GHz	Programmable dynamic metasurface antenna	Dynamic metasurface aperture	Reconfigurable	Programmable aperture for imaging and sensing; requires active control rather than a passive fixed multi-beam lens.
This work	**58–63 GHz**	**Passive multi-beam tailored GRIN Luneburg lens**	**Five commercial FMCW radar modules**	**Five beams**	**Commercial-radar-fed shared passive aperture with fabrication-aware non-radial GRIN phase tailoring for predefined multi-radar sector allocation.**

old, demonstrating practical sector-level discrimination with the TLL-integrated multi-radar platform. The experiment should be interpreted as a controlled threshold-based sector-detection measurement rather than a statistical classification study. Nevertheless, the absence of multi-channel activation for the tested target positions indicates reduced cross-sector ambiguity under the selected measurement conditions. Together with the 10–13 dB received-power enhancement, these results experimentally demonstrate the two principal system-level functions of the TLL: aperture-enhanced power delivery and sector-selective multi-radar sensing. Combined with the full-wave analysis, the measurements support the use of the TLL as a passive shared aperture for organizing radar responses around prescribed sensing sectors while preserving broadband power enhancement.

Table 1 compares the proposed work with representative radar-integrated aperture and lens- or metasurface-based enhancement methods. Prior approaches have demonstrated gain enhancement, low-profile integration, radome-loss reduction, near-field sensing enhancement, and programmable aperture operation, but generally employ single-feed or single-radar configurations or active/reconfigurable architectures. In contrast, the proposed TLL integrates five commercial FMCW radar modules with a shared passive volumetric GRIN aperture and employs non-radial dielectric tailoring to organize the simultaneous multiport response into predefined sensing sectors. The resulting architecture combines passive aperture enhancement, multi-sector beam allocation, and reduced cross-sector ambiguity within a single radar-integrated aperture.

5. Conclusion

This paper presented a passive multi-beam tailored GRIN Luneburg lens for millimeter-wave radar sensing using five commercial FMCW radar modules and a shared aperture. Although the conventional Luneburg lens provides effective aperture enhancement, its purely radial phase profile provides no additional degrees of freedom for organizing the multi-port aperture response under the defined five-port excitation condition. The proposed TLL introduces fabrication-aware non-radial volumetric phase control to modify the phase response of the radar-fed fields and organize the resulting multiport aperture response around five predefined sensing sectors, without mechanical scanning, phase shifters, or active beamforming.

Full-wave simulations showed that the TLL produces five dominant high-gain lobes near the prescribed directions of -56°, -28°, 0°, $+28^\circ$, and $+56^\circ$, with peak realized gains of approximately 20–22 dB. For the outer sectors, the angular allocation error is reduced from approximately 26°–29° with the CLL to about 2° with the TLL. The realized-gain reduction from single-port to simultaneous five-port excitation is also reduced from approximately 2.6 dB for the CLL to 0.5 dB for the TLL. Adjacent-channel analysis further shows frequency-selective isolation near the 60 GHz design frequency, where the transmission coefficients reach approximately -50 to -70 dB compared with approximately -38 to -41 dB for the radar-only configuration. This suppression is localized near the design frequency and does not restrict the full 58–63 GHz FMCW bandwidth available for ranging.

System-level measurements using the fabricated TLL demonstrated approximately 10–13 dB received-power enhancement across the 58–63 GHz operating band. Threshold-based measurements with a corner reflector further demonstrated sector-selective operation, with the radar channel corresponding to the tested target sector exceeding the detection threshold while the remaining channels stayed below it. Together, the simulated and measured results demonstrate that a fabrication-aware TLL can serve as a passive shared aperture for multiple commercial millimeter-wave radar modules, providing aperture enhancement and predefined spatial sectorization within a compact sensing front end. Future work will focus on improving aperture efficiency through optimized radar-to-lens integration and smaller feed modules, broadening the adjacent-channel isolation bandwidth, and extending the tailored GRIN design toward broadband multi-beam operation and real-time multi-target sensing.

Acknowledgment

The authors would like to acknowledge the support of the Wireless Sensors and Devices Lab (WSDL) at the University of Waterloo and the Royal Military College of Canada. Special thanks are also extended to Fortify Inc. for their contribution to the fabrication process and technical assistance throughout the development of this work.

References

[1] C. Li, Z. Peng, T.-Y. Huang, T. Fan, F.-K. Wang, T.-S. Horng, J.-M. Munoz-Ferreras, R. Gomez-Garcia, L. Ran, and J. Lin, "A review on recent progress of portable short-range noncontact microwave radar systems," *IEEE Transactions on Microwave Theory and Techniques*, vol. 65, no. 5, pp. 1692–1706, 2017.

[2] Y. Chen, J. Yuan, and J. Tang, "A high precision vital signs detection method based on millimeter wave radar," *Scientific Reports*, vol. 14, no. 1, p. 25535, 2024.

[3] M. O. Bagheri, A. Gharamohammadi, S. Abu-Sardanah, O. M. Ramahi, and G. Shaker, "Radar near-field sensing using metasurface for biomedical applications," *Communications Engineering*, vol. 3, no. 1, p. 51, 2024.

[4] X. Zhang, C. Liu, Y. Cheng, Z. Li, C. Xu, C. Huang, Y. Zhan, W. Bo, J. Xia, and W. Xu, "A comprehensive survey of research trends in mmwave technologies for medical applications," *Sensors*, vol. 25, no. 12, p. 3706, 2025.

[5] A. Gharamohammadi, M. O. Bagheri, S. Abu-Sardanah, M. M. Riad, H. Abedi, A. Ansariyan, K. Wang, A. Saragadam, D. Chumachenko, S. Abhari *et al.*, "Smart furniture using radar technology for cardiac health monitoring," *Scientific Reports*, vol. 15, no. 1, p. 1392, 2025.

[6] A. J. Fenn, D. H. Temme, W. P. Delaney, and W. E. Courtney, "The development of phased-array radar technology," *Lincoln laboratory journal*, vol. 12, no. 2, pp. 321–340, 2000.

[7] A. H. Naqvi and S. Lim, "Review of recent phased arrays for millimeter-wave wireless communication," *Sensors*, vol. 18, no. 10, p. 3194, 2018.

[8] Z. Ahmad, M. Chen, and S.-D. Bao, "Beampattern analysis of frequency diverse array radar: a review," *EURASIP Journal on Wireless Communications and Networking*, vol. 2021, no. 1, p. 189, 2021.

[9] D. Zheng, G.-B. Wu, Z. H. Jiang, W. Hong, C. H. Chan, and K. Wu, "Enabling beam-scanning antenna technologies for terahertz wireless systems: A review," *Fundamental Research*, vol. 5, no. 2, pp. 556–570, 2025.

[10] M. O. Bagheri, E. Y. Harmgarth, O. M. Ramahi, Y. M. Antar, and G. Shaker, "Uniformly 3d-printed low-cost hedgehog spherical lens antenna," *IEEE Open Journal of Antennas and Propagation*, 2025.

[11] H. Abedi, A. E. Omer, J. Hanna, A. Ansariyan, S. Ding, A. F. Perez, T. Paraschuk, P. P. Morita, J. Boger, A. Wong *et al.*, "On the use of an in-package dielectric lens antenna for radar-based applications," *IEEE Transactions on Components, Packaging and Manufacturing Technology*, vol. 14, no. 2, pp. 315–327, 2024.

[12] M. O. Bagheri, H. Abedi, and G. Shaker, "3d-printed dielectric rods for radar range enhancement," *Electronics*, vol. 12, no. 19, p. 4016, 2023.

[13] M. O. Bagheri, H. R. Hassani, and A. R. Sebak, "Stable phase-centre horn antenna using 3d printed dielectric rod

for aperture efficiency improvement of space-fed antennas," *IET Microwaves, Antennas & Propagation*, vol. 16, no. 14, pp. 888–897, 2022.

[14] M. O. Bagheri and G. Shaker, "Near-field enhancement of microstrip antenna using engineered superstrate for biomedical applications," in *2022 IEEE International Symposium on Antennas and Propagation and USNC-URSI Radio Science Meeting (AP-S/URSI)*. IEEE, 2022, pp. 1038–1039.

[15] M. O. Bagheri, H. Abedi, and G. Shaker, "Radar antenna gain improvement using 3d-printed dielectric lens and metamaterial-inspired superstrates," in *2021 IEEE 19th International Symposium on Antenna Technology and Applied Electromagnetics (ANTEM)*. IEEE, 2021, pp. 1–2.

[16] M. O. Bagheri, H. R. Hassani, and B. Rahmati, "Dual-band, dual-polarised metallic slot transmitarray antenna," *IET microwaves, antennas & propagation*, vol. 11, no. 3, pp. 402–409, 2017.

[17] M. O. Bagheri, O. M. Ramahi, and G. Shaker, "Metasurface for high-sensitivity radar sensing," in *2025 IEEE Microwaves, Antennas, and Propagation Conference (MAPCON)*. IEEE, 2025, pp. 1–4.

[18] ——, "Dual-band, dual independently-tunable near-field focus metasurface for advanced radar bio-sensor," in *2025 IEEE International Workshop on Antenna Technology (iWAT)*. IEEE, 2025, pp. 1–4.

[19] ——, "Metasurface-enhanced bio-sensing radar for advanced health monitoring," in *2024 IEEE International Symposium on Antennas and Propagation and INC/USNC-URSI Radio Science Meeting (AP-S/INC-USNC-URSI)*. IEEE, 2024, pp. 2473–2474.

[20] M. Ansari, B. Jones, and Y. J. Guo, "Spherical luneburg lens of layered structure with low anisotropy and low cost," *IEEE Transactions on Antennas and Propagation*, vol. 70, no. 6, pp. 4307–4318, 2022.

[21] Y. Li, L. Ge, M. Chen, Z. Zhang, Z. Li, and J. Wang, "Multibeam 3-d-printed luneburg lens fed by magnetoelectric dipole antennas for millimeter-wave mimo applications," *IEEE Transactions on Antennas and Propagation*, vol. 67, no. 5, pp. 2923–2933, 2019.

[22] P. Afanasyev, S. Matitsine, V. Sledkov, P. Lagoiski, L. Matytsine, T. DeMarco, and T.-T. Chia, "Multi-beam luneburg lens antenna for cellular communications," in *2015 9th European Conference on Antennas and Propagation (EuCAP)*. IEEE, 2015, pp. 1–4.

[23] X. Li, R. Feng, Q. Tan, J. Yi, S. Wang, F. He, and S. N. Burokur, "Additively-manufactured broadband metamaterial-based luneburg lens for flexible beam scanning," *Materials*, vol. 17, no. 12, p. 2847, 2024.

[24] M. O. Bagheri, E. Y. Harmgarth, H. Ramberg, O. M. Ramahi, Y. M. Antar, and G. Shaker, "Dielectric grin luneburg lens for enhanced radar sensing in communication systems," *IEEE Transactions on Microwave Theory and Techniques*, 2025.

[25] M. O. Bagheri, E. Y. Harmgarth, H. Ramberg, E. Biebl, and G. Shaker, "Radar antennas employing a modified dielectric grin luneburg lens," in *2024 IEEE MTT-S International Conference on Numerical Electromagnetic and Multiphysics Modeling and Optimization (NEMO)*. IEEE, 2024, pp. 1–3.

[26] M. O. Bagheri, H. Ramberg, Y. M. Antar, and G. Shaker, "Computational synthesis of tailored grin luneburg lenses for mm-wave radar integration," in *2026 International Applied Computational Electromagnetics Society Symposium (ACES)*. IEEE, 2026, pp. 1–2.

[27] M. O. Bagheri, V. Leong, J. Chow, J. Visser, and G. Shaker, "Modified grin luneburg lens for high-efficiency millimeter-wave multi-radar sensing," in *2026 20th European Conference on Antennas and Propagation (EuCAP)*. IEEE, 2026, pp. 1–3.

[28] P. Hallbjorner, Z. He, S. Bruce, and S. Cheng, "Low-profile 77-ghz lens antenna with array feeder," *IEEE Antennas and wireless propagation letters*, vol. 11, pp. 205–207, 2012.

[29] C. Kohlberger, R. Hüttner, C. Wagner, and A. Stelzer, "Metamaterial lenses for monostatic and bistatic 77 ghz radar systems," *International journal of microwave and wireless technologies*, vol. 15, no. 6, pp. 1021–1026, 2023.

[30] W. Yang, K. Chen, and Y. Feng, "A metasurface-based folded transmitarray antenna for 77 ghz automotive radar applications," in *2022 IEEE MTT-S International Microwave Workshop Series on Advanced Materials and Processes for RF and THz Applications (IMWS-AMP)*. IEEE, 2022, pp. 1–3.

[31] R. Tang, W. Gao, R. Yu, Y. Zhan, H. Zhang, and J. Zhang, "Dual-band huygens' metasurface lens antenna for automotive millimeter-wave radar," *IEEE Antennas and Wireless Propagation Letters*, 2025.

[32] I. Moon, W. Kim, Y. Seo, and S. Kahng, "A metamaterial surface avoiding loss from the radome for a millimeter-wave signal-sensing array antenna," *Sensors*, vol. 24, no. 3, 2024.

[33] S. R. Wang, Z. Y. Chen, S. N. Chen, J. Y. Dai, J. W. Zhang, Z. J. Qi, L. J. Wu, M. K. Sun, Q. Y. Zhou, H. D. Li *et al.*, "Simplified radar architecture based on information metasurface," *Nature Communications*, vol. 16, no. 1, p. 6505, 2025.

[34] A. Jabbar, M. Elsayed, J. U. R. Kazim, Z. Pang, J. Le Kernec, M. A. Imran, Q. H. Abbasi, and M. Ur-Rehman, "60 ghz programmable dynamic metasurface antenna (dma) for next-generation communication, sensing, and imaging applications: From concept to prototype," *IEEE Open Journal of Antennas and Propagation*, vol. 5, no. 3, pp. 705–726, 2024.